Research Square

Preprints are preliminary reports that have not undergone peer review.
They should not be considered conclusive, used to inform clinical practice,
or referenced by the media as validated information.

Structural, optoelectronic, and thermoelectronic properties of transition-metal-based dichalcogenides MoX2 (X = S, Se, Te) as 2D semiconductors for photoelectronic applications

M. Musa Saad H.-E.

141261@qu.edu.sa

Qassim University

B. O. Alsobhi

Taibah University

A. Almeshal

Qassim University

Article

Keywords: 2D transition-metals MoX2, Semiconductors, Direct band-gap, Optical responses, GGA-mBJ

Posted Date: September 14th, 2026

DOI: https://doi.org/10.21203/rs.3.rs-10710050/v1

License: This work is licensed under a Creative Commons Attribution 4.0 International License.
Read Full License

Additional Declarations: No competing interests reported.

Structural, optoelectronic, and thermoelectronic properties of transition-metal-based dichalcogenides MoX_2 (X = S, Se, Te) as 2D semiconductors for photoelectronic applications

M. Musa Saad H.-E. [a,*], B. O. Alsobhi [b], and A. Almeshal [a]

[a] Department of Physics, College of Science, Qassim University, Buridah, 51452, Saudi Arabia

[b] Physics Department, Faculty of Science, Taibah University, Al-Madinah al-Munawarah, Saudi Arabia

[*] Corresponding Author: Email: 141261@qu.edu.sa; ORCID: 0000-0002-6338-0915

Abstract

Two-dimensional (2D) transition-metal dichalcogenides (TMDs) MoX_2 with (X = S, Se, Te) are systematically investigated using density functional theory (DFT) combined with Boltzmann transport theory within the relaxation-time approximation. The structural, optoelectronic, and thermoelectronic properties are analyzed using the generalized gradient approximation (GGA) and GGA-modified Becke–Johnson (GGA-mBJ) potential. The optimized structures and formation energies confirm that all MoX_2 compounds are thermodynamically stable in the hexagonal symmetry with $P6_3/mmc$ phase. Electronic band-structures and density of states calculations reveal semiconducting characteristics, with direct band gaps decreasing from (X = S to Te) as the chalcogen atomic size increases. The calculated optical parameters, including dielectric function, absorption coefficient, optical conductivity, refractive index, reflectivity, and energy-loss function, show pronounced optical absorption in the visible–ultraviolet region, suggesting that MoX_2 monolayers may have potential for photoelectronic, photovoltaic, and photodetection applications. Thermoelectronic analysis further reveals that chalcogen substitution strongly affects the charge-carrier transport and thermoelectronic efficiency. The studied MoX_2 monolayers exhibit low thermal conductivity and enhanced electrical transport properties, leading to favorable thermoelectronic figure of merit ($ZT = 1.083$, 0.991, and 0.988) for MoS_2, $MoSe_2$, and $MoTe_2$, respectively. The present findings highlight the potential of these layered MoX_2 compounds for future photoelectronic, thermoelectronic, and energy-conversion technologies.

Keywords: 2D transition-metals MoX_2; Semiconductors; Direct band-gap; Optical responses; GGA-mBJ.

1. Introduction

Low-dimensional materials, particularly two-dimensional (2D) layered systems, have attracted widespread interest due to their distinct physical and chemical properties compared with their bulk counterparts. The reduction in dimensionality leads to quantum confinement effects,

altered electronic band structures, and enhanced surface-to-volume ratios, which collectively enable novel functionalities not accessible in three-dimensional (3D) materials. Since the successful isolation of graphene [1], research in this field has expanded rapidly to include a broad spectrum of 2D materials with diverse composition and bonding characteristics [1-5]. Among these, elemental monolayers such as silicene, germanene, phosphorene, arsenene, and antimonene have demonstrated tunable electronic properties ranging from metallic to semiconducting behavior, making them promising for nanoelectronics applications [6-8]. Beyond elemental systems, binary layered compounds, particularly transition-metal dichalcogenides (TMDs), have emerged as a central class of semiconducting 2D materials. Representative examples such as molybdenum disulfide (MoS_2) and tungsten diselenide (WSe_2) exhibit sizeable band gaps, strong spin-orbit coupling, and pronounced light–matter interactions, which are highly desirable for optoelectronic and photonic devices [9-12]. Furthermore, recent theoretical studies have demonstrated that compositional tuning and defect engineering can significantly modify the structural, electronic, and optical properties of such materials [13,14].

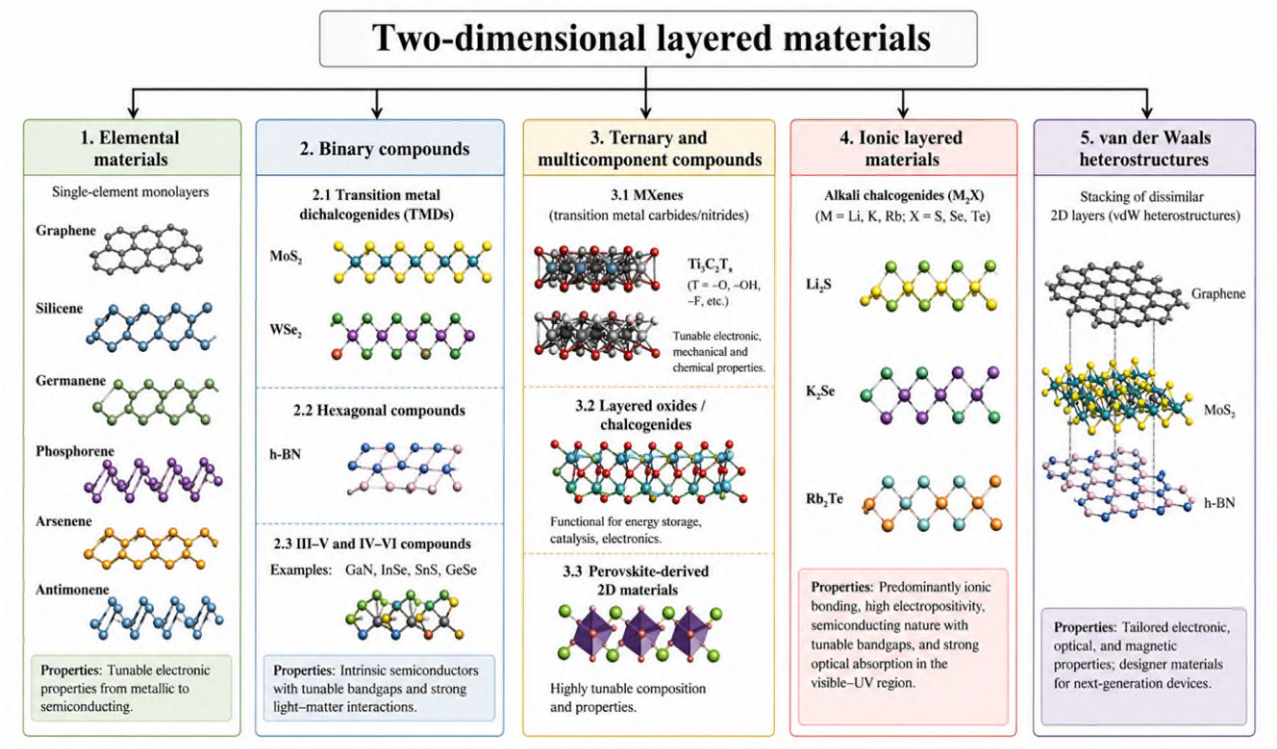


Figure 1. Schematic classification of two-dimensional (2D) layered materials along with their principal chemical and physical characteristics. The materials are broadly grouped into five categories: (1) elemental monolayers, (2) binary compounds, including transition-metal dichalcogenides (TMDs), hexagonal systems (h-BN), and III–V/IV–VI materials, (3) ternary and multicomponent structures, (4) ionic layered compounds, and (5) van der Waals heterostructures. These classes exhibit a wide spectrum of physical properties, supporting diverse applications in electronics, energy storage, catalysis, and optoelectronics technologies.

In addition, insulating layered materials such as hexagonal boron nitride (h-BN) play a crucial role as dielectric substrates and encapsulation layers due to their chemical stability and atomically smooth surfaces [15]. More complex families, including MXenes, further extend the functionality of 2D systems through their rich surface chemistry and tunable electronic properties, enabling applications in energy storage, catalysis, and sensing [16]. Recently, ionic 2D compounds, particularly alkali chalcogenides (M_2X), have also gained attention due to their strong charge transfer and notable optical responses [17]. Collectively, these classes highlight the diversity of the 2D materials landscape and their significant potential for next-generation electronic, energy, and optoelectronic technologies. A general classification of 2D layered materials, along with their key chemical and physical characteristics, is presented in Figure 1.

Transition-metal dichalcogenides (TMDs) represent one of the most extensively studied categories within this family. These materials generally adopt the chemical formula MX_2 (M = transition metal; X = chalcogen) and exhibit layered structures composed of a transition-metal (M) plane sandwiched between two chalcogen (X) layers. Strong covalent bonding within the layers and weak van der Waals (vdW) interactions between them enable mechanical exfoliation and the formation of stable monolayers [9,18,19]. Importantly, their physical properties can be effectively tuned through variations in chemical composition, layer thickness, strain, and external conditions such as temperature, pressure or chemical intercalation [20,21]. Intercalation processes, involving species such as alkali metals, halogens, or organic molecules, can significantly modify the structural, electronic, optical, and magnetic properties of these systems and may also facilitate exfoliation into single-layer sheets [21].

Moreover, TMD-based heterostructures and Janus materials have recently attracted significant attention due to their enhanced electronic and optical performance, offering additional flexibility in device design [22]. These materials also exhibit potential in emerging fields such as biomedical applications and sensing technologies [23]. Extensive experimental and theoretical studies have demonstrated the versatility of TMDs across a wide range of applications, including nanoelectronics, catalysis, and energy storage [23-26]. Among TMDs, compounds based on molybdenum and tungsten have attracted particular attention due to their favorable semiconducting characteristics and strong optical absorption in the visible range. Materials such as MoS_2, $MoSe_2$, WS_2, and WSe_2 exhibit layer-dependent band gaps and robust excitonic effects, making them suitable for applications in photovoltaics, photodetectors, and flexible optoelectronics [10,12]. Furthermore, related 2D systems such as Pt-based

dichalcogenides, e.g., PtS_2 and $PtSe_2$, have been reported to display high optical conductivity and efficient light absorption spanning the visible to ultraviolet regions [13,19,23,24].

Motivated by these promising properties, the present study systematically investigates the influence of transition-metal (M) and chalcogen (X) constituents on the structural, optoelectronic, and thermoelectronic behavior of 2D TMCs with the general chemical formula MoX_2 (X = S, Se, Te). Different crystallographic phases of these molybdenum sulfides, selenides, and tellurides monolayer MoX_2 are considered, and their stability is evaluated through structural optimization and formation energies analysis. The electronic band structures and densities of states are analyzed to determine their suitability for semiconducting applications. In addition, optical properties are explored to evaluate light absorption and optical transitions, and thermoelectronic performance is investigated based on calculated transport parameters. The remainder of this paper is organized as follows. First, the computational methodology is described. Next, the optimized structures and stability are presented and discussed. This is followed by an analysis of formation energies and thermodynamic properties. Subsequently, the electronic and optical properties are examined in detail. Finally, the thermoelectronic and transport characteristics are evaluated, and key conclusions are drawn.

2. Computational methodology

The present first-principles density functional theory (DFT) calculations were performed by using the full-potential linearized augmented plane wave (FP-LAPW) method as implemented in the Wien2k computational package [27,28]. These DFT calculations were carried out to evaluate the structural and different physical properties of the studied materials MoX_2 (X = S, Se, Te). In this study, the exchange-correlation energy was treated using the generalized gradient approximation (GGA) [28,29]. The structural optimization of the total energy with respect to different values of unit cell volume has been performed using the GGA calculations based on the Perdew–Burke–Ernzerhof (GGA-PBE) potential [30]. Moreover, the electronic and optical properties were investigated by employing the modified Becke–Johnson potential (GGA-mBJ) [31], which gives more accurate description of electronic structures and band gaps that the conventional GGA-PBE approach.

In FP-LAPW method, the space of MoX_2 crystals is divided into non-overlapping atomic muffin-tin spheres (MTSs) which are separated by an interstitial region (IR). Thus, the basis functions inside MTSs are expanded into spherical harmonic function, while the Fourier series are expanded in the IR [32]. In current calculations, the basis functions inside MTSs are expanded up to ($R_{MT}K_{Max} = 7$). Here, R_{MT} denotes the smallest atomic radius of MTSs, and K_{Max} is the

largest reciprocal lattice vector used in the plane wave (PLW) expansion [28]. The smallest atomic radii R_{MT} of MTSs are input as 2.32/1.99 a.u. for Mo/S, 2.26/2.26 a.u. for Mo/Se, and 2.37/2.50 a.u. for Mo/Te atoms in all these FP-LAPW calculations. Also, the maximum quantum orbital number for the plane wave PLW expansion inside these atomic MT spheres is designated as ($L_{max} = 10$). The cutoff energy is input as (E_{cutoff} = -7 Ry), which refers to separation energy between the core and valence electrons in the crystal structure of MoX_2. To describe the limits of the largest vector in plane wave PLW expansion, the Fourier expansion parameter is chosen as ($G_{max} = 12$) for the charge density. In addition, the energy and charge convergences are input as 0.0001 Ry and 0.001e, respectively, in the self-consistent (scf) calculations. For the Brillouin zone (BZ) integration, the scf and GGA calculations for all structural, electronic, and optical properties were carried out by choosing the grid as (12×10×22) with a total number of k points ($K_{points} = 3000$) in first BZ. Furthermore, the thermoelectric and transport properties are evaluated using the BoltzTraP program, which is interfaced with the Wien2k code [33].

3. Results and discussion

3.1. 2D crystal structure and stability properties

Although the individual structural, electronic, or optical properties of MoS_2, $MoSe_2$, and $MoTe_2$ compounds have been reported previously, comprehensive investigations that consistently combine structural optimization, electronic structure, optical response, and thermoelectric transport within a unified first-principles framework remain relatively limited. In the present work, all members of the 2D MoX_2 (X = S, Se, Te) family are examined using identical computational parameters, allowing direct comparison of the influence of chalcogen substitution on multiple physical properties. This unified approach reveals systematic correlations between lattice expansion, band-gap reduction, dielectric response, optical absorption, carrier transport, and thermoelectric efficiently, thereby providing a coherent understanding of composition-dependent property evolution. Such comparative analysis offers useful design guidelines for selecting appropriate MoX_2 compounds for future optoelectronic, photovoltaic, and thermoelectric applications.

The 2D transition-metal dichalcogenides (TMDs) MoX_2 (X = S, Se, Te) crystallize in the hexagonal structure with space group $P6_3/mmc$ (No. 194), which is commonly observed in both bulk and layered phases. The corresponding 2D crystal structures for the MoX_2 compounds are illustrated in Figure 2. In this structure, the Wyckoff sites and atomic positions in the $P6_3/mmc$ unit cell of these compounds are as follows: the transition metal Mo atoms sit at $2d$ with

fractional coordinates (⅓, ⅔, ¾) and (⅔, ⅓, ¼), whereas the chalcogen atoms X (X = S, Se, Te) occupy the $4f$ site with coordinates (⅓, ⅔, z), (⅔, ⅓, ½+z), (⅔, ⅓, 1-z), and (⅓, ⅔, ½-z) positions. The optimized internal parameter z is listed in Table 1. In addition, the lattice constants per the essential unit cell of these $P6_3/mmc$ crystal structures in all MoX_2 systems satisfy the relation $a = b \neq c$ with $\alpha = \beta = 90°$, and $\gamma = 120°$.

Before the scheming the physical properties of the 2D-TMCs monolayer MoX_2 (X = S, Se, Te), structural optimization was carried out to determine the ground-state energy (E_0), equilibrium lattice parameters, and unit-cell volumes. The structural optimization calculations were performed using the FP-LAPW method implemented in the Wien2k computational package. The variation of total energy (E) as a function of the unit-cell volume (V) is shown in Figure 3, where the obtained $E - V$ data were fitted using the Birch–Murnaghan equation of state [27,28,34]. The optimized structural parameters of the investigated systems, including the ground-state energy (E_0), equilibrium volume (V_0), lattice constants (a_0, b_0, c_0), bulk modulus (B_0), and pressure derivative of the bulk modulus (B′), are summarized in Table 1.

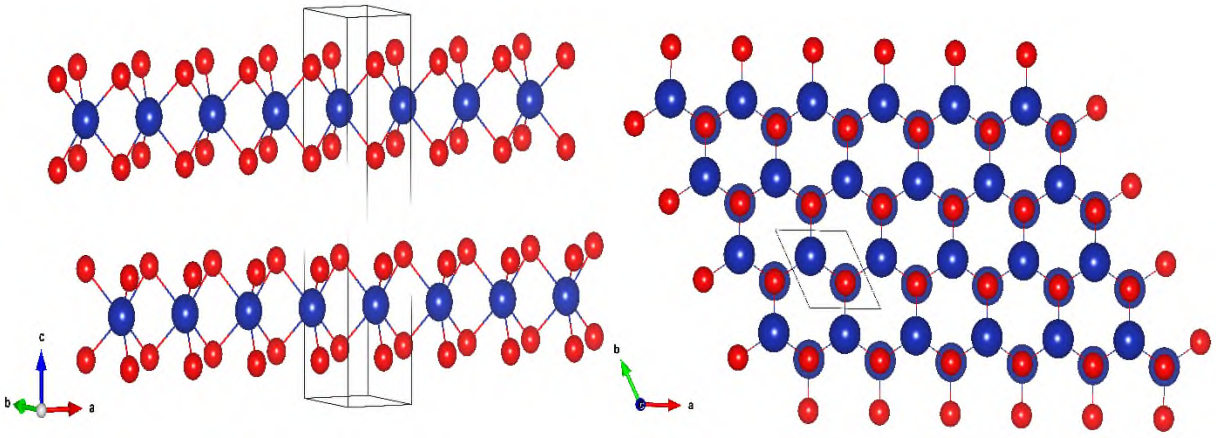


Figure 2. Side view (left) and top view (right) of the molybdenum dichalcogenide monolayers MoX_2 (X = S, Se, Te). Mo atoms are represented by blue spheres, and X atoms are sketched by red spheres.

Table 1. The optimized unit-cell parameters, lattice constants (a_0, b_0, c_0), equilibrium volumes (V_0), fractional coordinates (z), ground-state energy (E_0), and bulk modulus (B_0), for the 2D monolayer MoX_2 (X = S, Se, Te) together with available experimental and theoretical values.

MoX_2	$a_0 = b_0$ (Å)	c_0 (Å)	c_0/a_0	V_0 (Å³)	B_0 (GPa)	E_0 (Ry)	z
MoS_2	3.191	13.28	4.162	117.1	133.3	-19392.3	0.633
	3.161 [35], 3.162 [36], 3.210 [42]	12.30 [35], 12.31 [36], 12.44 [42]	3.892 [35], 3.894 [36], 3.875 [42]				
$MoSe_2$	3.320	13.54	4.078	129.3	114.5	-35640.5	0.872
	3.294 [36], 3.283 [37], , 3.330 [42]	13.00 [36], 12.92 [37], 13.05 [42]	3.894 [36], 3.935 [37], 3.919 [42]				
$MoTe_2$	3.571	14.65	4.102	161.8	88.31	-70573.7	0.628

	3.518 [36], 3.552 [37], 3.550 [38], 3.540 [42]	14.07 [36], 13.97 [37], 13.88 [38], 14.01 [42]	3.999 [36], 3.933 [38], 3.910 [38], 3.958 [42]				

The optimized magnitudes show that the ground-state energy E_0 of MoX_2 regularly increases when the halogen X-site changes from X = S to Se and then to Te. This behavior can be attributed to the increase in total energy per unit cell as well as the larger atomic radius of the substituted halogen atom. From the $E - V$ curves shown in Figure 3, the equilibrium hexagonal lattice constants (a_0, b_0, c_0) for each monolayer MoX_2 were determined from the corresponding ground-state parameters. It is observed that replacing S with Se and Te at the X-site leads to a noticeable increase in both the lattice constants and the equilibrium unit-cell volume V_0. This trend is consistent with the periodic variation in atomic size of the X atoms (X = S, Se, Te) forming these TMCs. The hexagonal crystal structures and optimized parameters for these 2D systems agrees well with the previously reported results [35-43]. In contrast, the bulk modulus B_0 values show a decreasing trend from S to Te, which can be mainly explained by the gradual increase in atomic radius that weakens the bonding strength within the crystal lattice of MoX_2. Moreover, the three MoX_2 compounds show equal B′ value of 5.0.

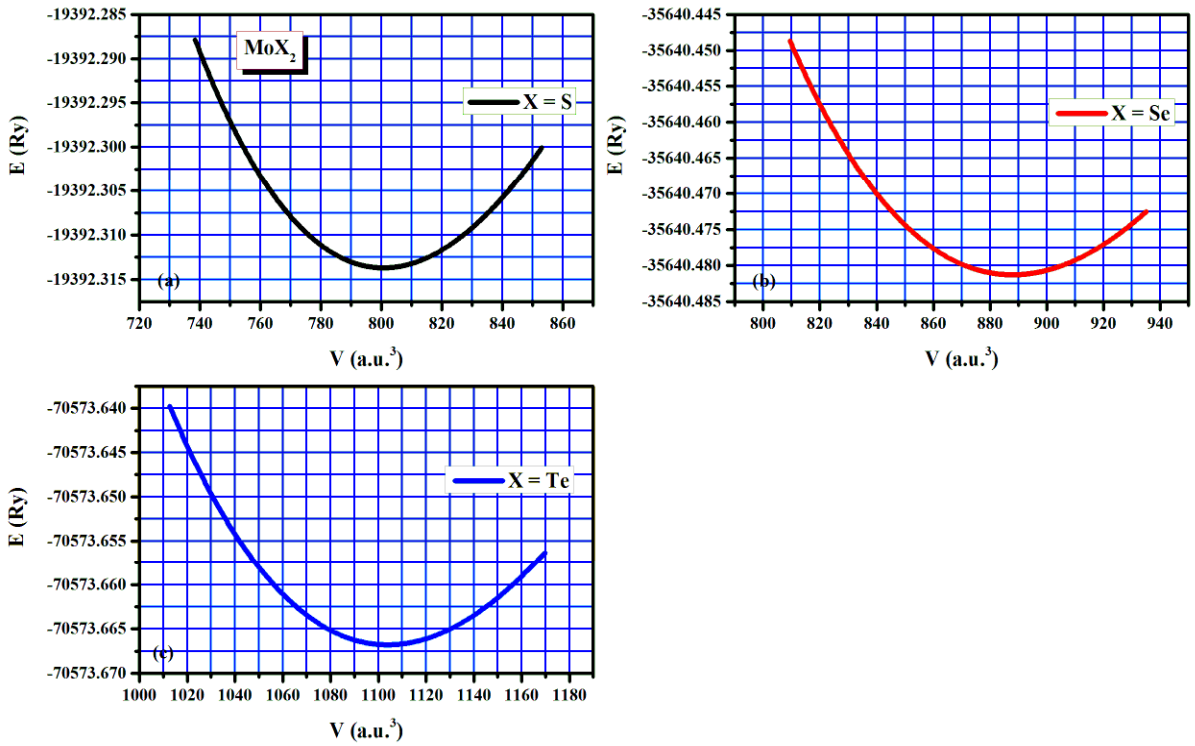


Figure 3. The structural optimization curves of 2D monolayer MoX_2 (X = S, Se, Te) in a bulk phase.

The calculated atomic bond distances of Mo–X are 2.464, 2.532, and 2.730 Å, and for X–X bonds are 3.190, 3.310, and 3.580 Å, respectively. Whereas, the bond angles X–Mo–X are 80.7°, 81.6°,

and 81.9°. The chemical bonding in MoX_2 is characterized by a dual nature; strong intralayer covalent bonding between molybdenum and chalcogen atoms (Mo–X) within the molecular sandwiches (X–Mo–X) and weak intermolecular vdW forces between the adjacent chalcogen layers (X–X). This structural feature makes easily to produce out 2D layers forms from the corresponding TMCs systems [41,44]. The unit cell of MoX_2 compounds contains two chalcogen atoms X site at the same position in the hexagonal lattice, whereas the molybdenum atoms Mo occupy the opposite sites. Thermodynamic stability is a key factor governing the applicability of organic and inorganic materials in energy-related devices, particularly, solar-energy conversion systems [32]. To evaluate the stability of investigated MoX_2 compounds, the formation energy (E_f) was calculated using: $E_f = E(MoX_2) - E(Mo) - 2E(X)$. The obtained negative formation energies confirm that all MoX_2 compounds are thermodynamically stable and experimentally synthesizable [45]. The calculated values of E_f per formula unit MoX_2 are -2.245, -1.305, and -1.115 eV for X = S, Se, and Te, respectively. These negative values indicate that the crystal structures of molybdenite MoX_2 are energetically more stable than their constituent atoms at zero temperature. Moreover, tellurides, $MoTe_2$, exhibits relatively higher structural stability than the corresponding sulfides and selenides compounds, and MoS_2 and $MoSe_2$, respectively.

3.2. Electronic properties

A detailed and deep understanding of the electronic properties is essential aspect for well describing the physical behavior of complex materials because the optoelectronic, thermoelectronic and charge-carrier transport properties are strongly governed by their electronic structures. In particular, efficient optoelectronic and thermoelectronic materials require suitable electronic band gaps to achieve strong optical absorption together with favorable power factor and electrical conductivity. Therefore, the electronic structures and semiconducting characteristics of the investigated 2D-TMCs MoX_2 (X = S, Se, Te) are analyzed in detail in this part. Figures 4-6 show the calculated density of states (DOS) and electronic band structures of MoX_2 monolayers obtained using the GGA-mBJ exchange-correlation approach, which provides improved prediction of the electronic structures and band-gap values. Our GGA-mBJ calculations results confirm that all investigated 2D- MoX_2 monolayers exhibit direct semiconducting behavior. Table 2 summarizes the electronic band gap (E_g) values of studied monolayers MoX_2 together with the previous experimental and theoretical results.

The theoretical electronic band-structures are plotted in Figure 4 along the high-symmetry directions Γ–M–K–Γ–A. The obtained results reveal that all investigated monolayer MoX_2

materials exhibit similar semiconducting behavior with direct band gaps. We can clearly see that the valence band maximum (VBM) and conduction band minimum (CBM) limit the extent of this band gap. The positions of VBM and CBM confirm the corresponding wave-vector values for these hexagonal crystal structures. Both the VBM and CBM in these MoX_2 compounds are located at the *K* point. Because of the similar electronic configuration of the constituent atoms, the three compounds display comparable band-dispersion features, although $MoTe_2$ system exhibits relatively dense electronic bands due to the heavier Te atom. We know that the electronic configuration of constituent atoms of the MoX_2 systems are as follows: Mo: $[Kr]^{36}\ 5s^1\ 4d^5$, S: $[Ne]^{10}\ 3s^2\ 3p^4$, Se: $[Ar]^{18}\ 4s^2\ 3d^{10}\ 4p^4$, and Te: $[Kr]^{36}\ 5s^2\ 4d^{10}\ 5p^4$. These configurations govern the electronic structures of MoX_2.

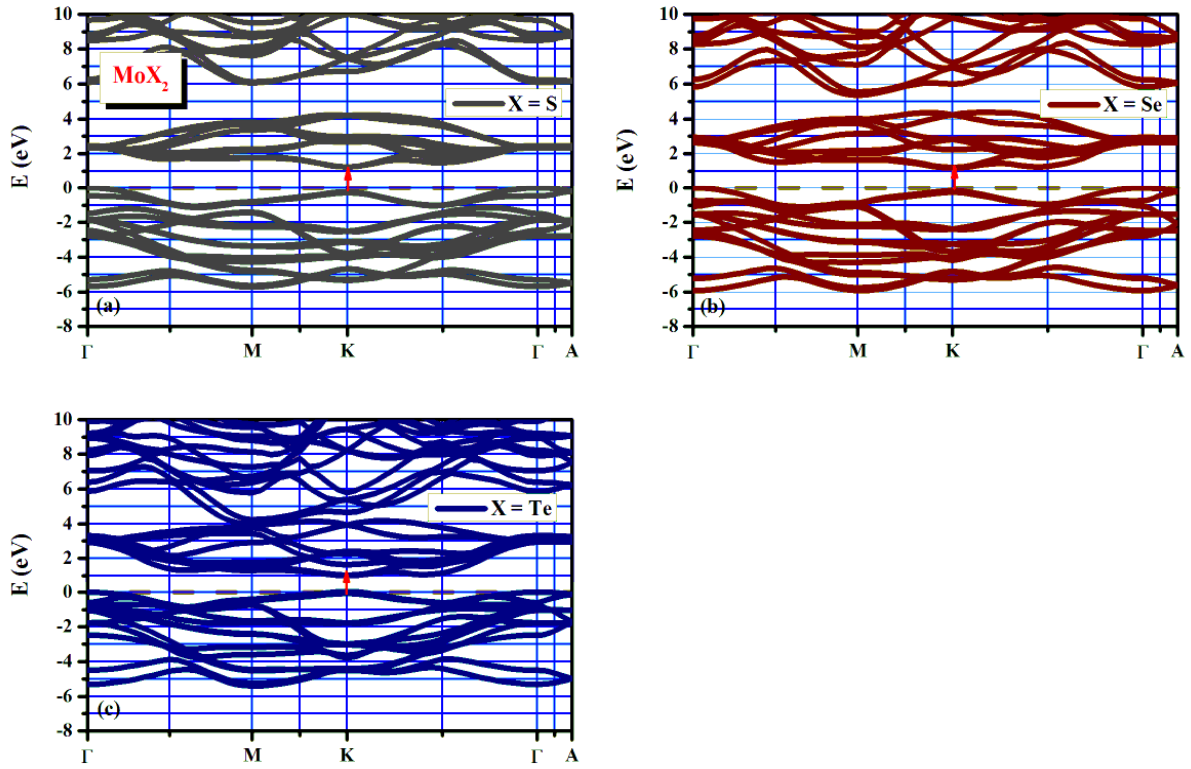
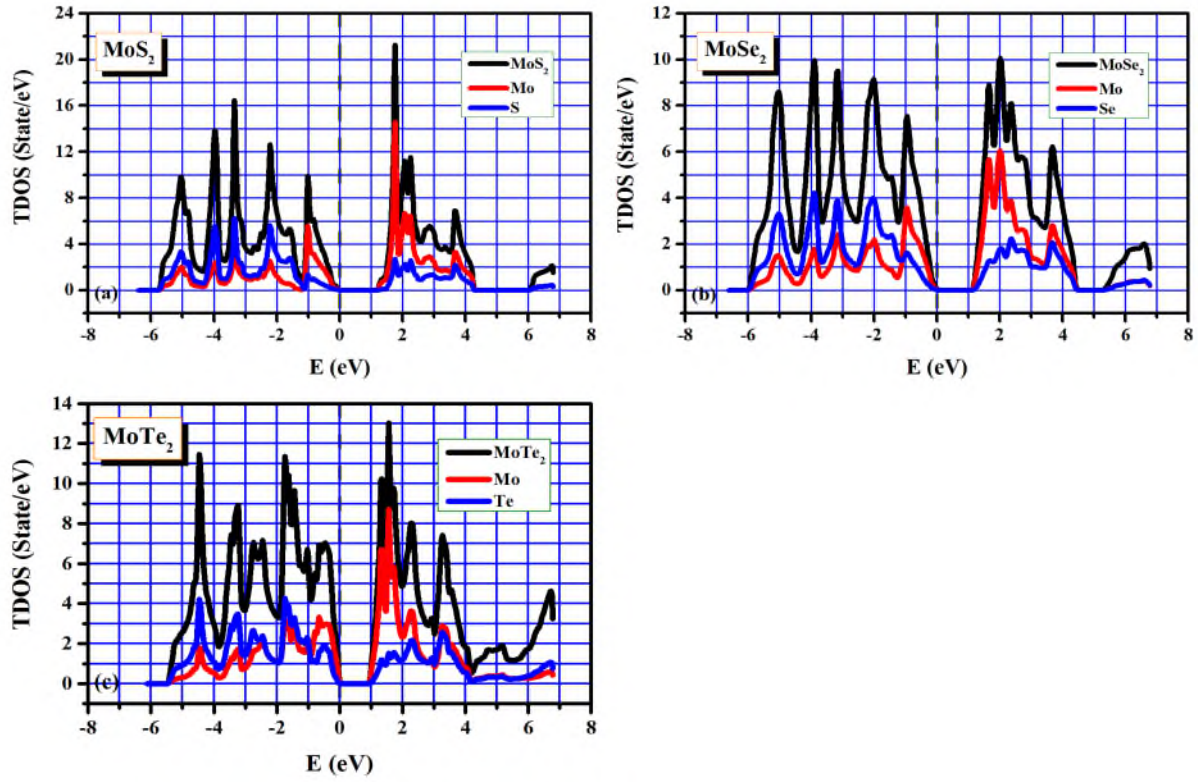
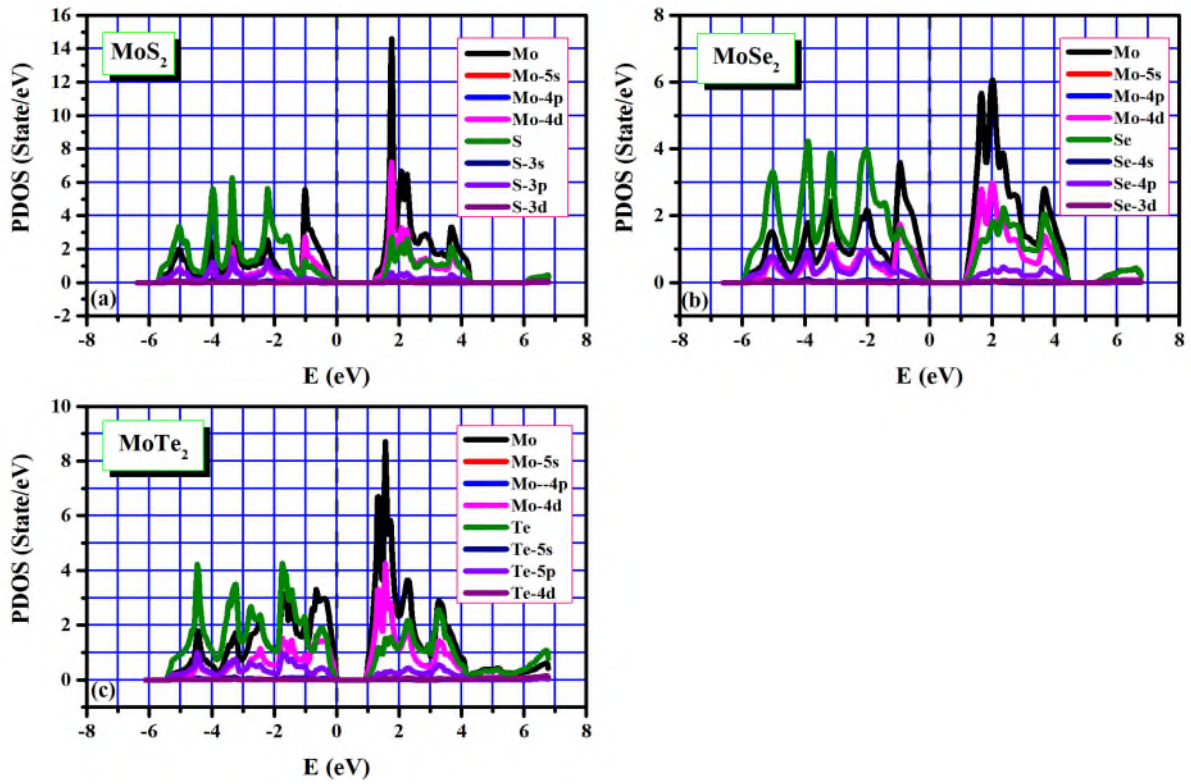


Figure 4. GGA-mBJ calculations of the electronic band structures of MoX_2 (X = S, Se, Te), along the high symmetry directions. The horizontal dashed line represents the Fermi level ($E_F = 0$ eV).



Figures 5. The GGA-mBJ calculation of the electronic total density of states (TDOS) of MoX_2, Mo, and X (X = S, Se, Te). The vertical dashed line characterises the Fermi level ($E_F = 0$ eV).

Table 2 shows that the calculated band gap E_g values of MoX_2 are about 1.196/1.295 eV for X = S, 1.030/1.235 eV for X = Se, and 0.930/1.039 eV for X = Te, from GGA-PBE/GGA-mBJ. The direct nature and E_g values obtained using the GGA-mBJ potential show better agreement with the experimental measurements using the photoacoustic spectroscopy technique; 1.230/1.370, 1.090/1.250, and 1.000/0.890 eV, respectively [43,44]. In addition, the values and direct nature of band gaps E_g are consistent with the earlier theoretical studies on these 2D materials [37,41]. Here, we observe that the GGA-PBE calculations, 1.196, 1.030, and 0.930 eV, usually underestimate the band-gap E_g values compared with experiments and more accurate theoretically methods. The present results indicate that the E_g values of MoX_2 are strongly affected by both the ionic radius of the X-site and the choice of GGA functional, demonstrating the sensitivity of electronic structure to structural and computational parameters. The existence of narrow band gap is a key requirement for determining the suitability of these 2D-MoX_2 materials for photoelectronic and related semiconductor applications.



Figures 6. The projected partial densities of states (PDOS) of Mo and X (X = S, Se, Te). The vertical dashed line characterises the Fermi level ($E_F = 0$ eV).

Moreover, the calculated total density of states (TDOS) shown in Figure 5 is fully consistent with the electronic band structures presented in Figure 4 for all investigated 2D-MoX_2 monolayers. As illustrated in the figure, all monolayers MoX_2 exhibit a clear semiconducting behavior with relatively narrow energy gaps E_g beyond the Fermi level ($E_F = 0$ eV), as summarized in Table 2. To further identify the atomic orbitals responsible for the formation of band edges, the partial densities of states (PDOSs) were also analyzed. Figure 6 shows the calculated different PDOS spectra of s, p, and d orbitals near the E_F. From the projected PDOSs of MoX_2, the VBM mostly originated from the orbital hybridization of the states Mo-4d–X-p (S-3p, Se-4p, and Te-5p). Similarly, these d–p states primely form the CBM but by high contributions in front of E_F. Therefore, the partial contributions of X-site around the E_F remains relatively small, as reflected by the low atomic TDOS intensity in this energy region. Nevertheless, the chalcogen X atoms play an essential role in stabilizing the crystal structure and maintaining charge balance within the MoX_2 monolayers. The obtained TDOS and PDOS features and corresponding electronic behavior are consistent with previously reported DFT studies on layered MoX_2 systems [36,41,42]. The overall similarity in the shape and distributions of TDOSs and PDOSs among the three MoX_2 monolayers is mainly attributed to

the substitutions of chalcogen S, Se, and Te at the chalcogen site, which does not significantly alter the electronic states near the band edges of the parent structure.

Table 2. The calculated band-gap energy E_g and basic optoelectronic parameters, including the static values of dielectric constant $\varepsilon_1(0)$, refractive index $n(0)$, and reflectively $R(0)$, and the maximum absorption $\alpha_{max}(\omega)$ at low/high energies $E(\alpha_{max})$, of MoX_2 (X = S, Se, Te) with their previous experimental and theoretical results.

MoX_2	E_g		$\varepsilon_1(0)$	$n(0)$	$R(0)$	$\alpha_{max}(\omega)$	$E(\alpha_{max})$ (eV)
	GGA-PBE	GGA-mBJ					
MoS_2	1.196	1.295	14.40	3.793	0.337	109.6/203.8	2.81/12.0
	1.590 [42], 1.230 [43]						
$MoSe_2$	1.030	1.235	15.61	4.008	0.361	153.7/201.1	5.94/11.5
	1.330 [42], 1.090 [43]						
$MoTe_2$	0.930	1.039	18.91	4.365	0.395	156.4/190.1	5.22/10.0
	0.930 [42], 1.00 [38,43]						

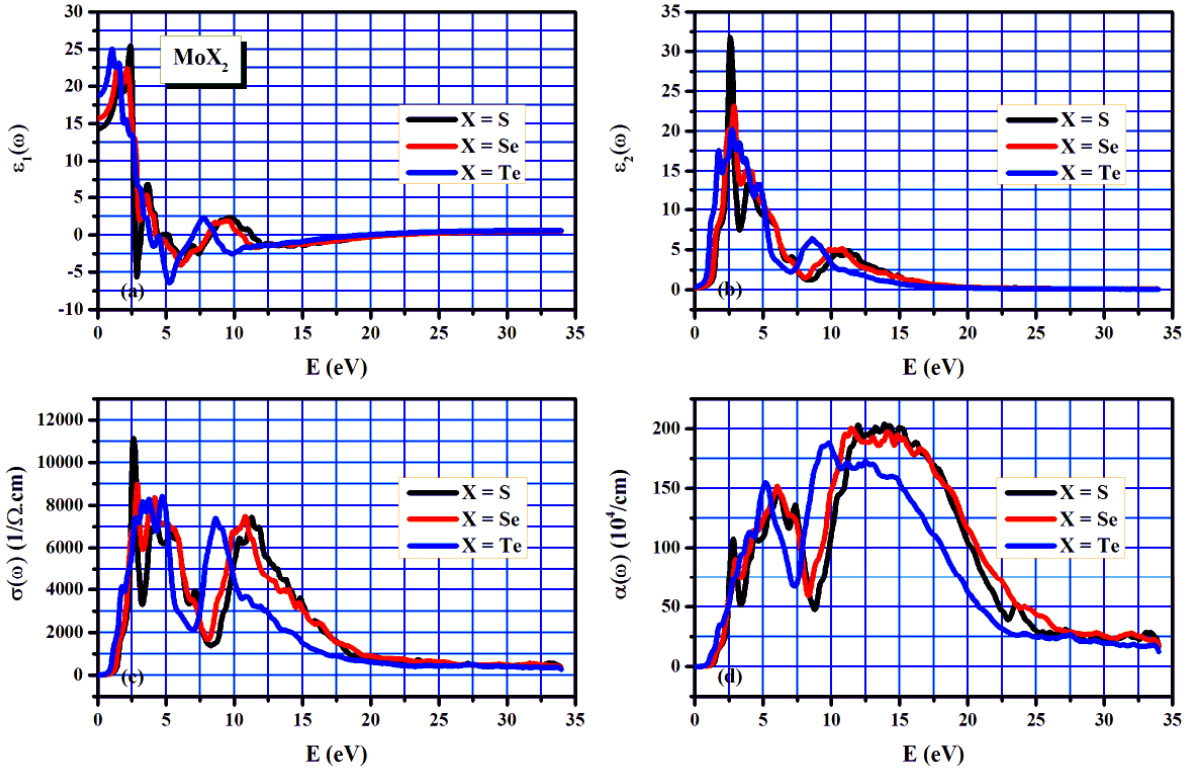
3.3. Optoelectronic properties

Highly efficient optoelectronic materials need strong interactions with electromagnetic energy to achieve effective light absorption and high charge-carrier transport properties. The main optoelectronic properties of the studied molybdenum monolayers MoX_2 (X = S, Se, Te) were analyzed and investigated based on their dielectric function $\varepsilon(\omega) = \varepsilon_1(\omega) + i\varepsilon_2(\omega)$. Her, the real part $\varepsilon_1(\omega)$ describes the energy storage, while the imaginary part $\varepsilon_2(\omega)$ represents optical absorption arising from the electronic intraband transitions [32,45]. The optical properties were calculated using the GGA-mBJ approach, which provides improved electronic-band-gap predictions. According to the Penn model, the static dielectric constant, 14.40, 15.61, and 18.91, is inversely related to the band gap: $\varepsilon_1(0) = 1 + \left(\hbar\omega_p/E_g\right)^2$ [32]. The calculated dielectric spectra of $\varepsilon_1(\omega)$ and $\varepsilon_2(\omega)$ shown in Figure 7(a,b) reveal strong optical activity of MoX_2 in the visible and near-infrared regions, with pronounced peaks originating from transitions between the valence and conduction bands [46-48]. The calculated $\varepsilon_1(\omega)$ peaks are 26.17 at 2.46 eV, 22.65 at 2.22 eV, and 25.30 at 1.02 eV for MoX_2, respectively. Whereas the corresponding $\varepsilon_2(\omega)$ peaks are 31.91, 23.57, and 20.68 emerge at 2.56, 2.80, and 2.75 eV, respectively. The absorption edge shifts systematically from MoS_2 to $MoTe_2$ due to the reduction in band gap with increasing chalcogen atomic size. The enhanced dielectric response and strong low-energy absorption suggest that these layered materials may have potential for optoelectronic, photovoltaic, and photodetection applications.

The optical conductivity spectra $\sigma(\omega)$ of MoX_2 (X = S, Se, Te) were calculated using the GGA-mBJ method are presented in Figure 7(c). Optical conductivity is directly related to the

imaginary part of the dielectric constant $\varepsilon_2(\omega)$: $\sigma(\omega) = \frac{\omega}{4\pi}\varepsilon_2(\omega)$. Since $\varepsilon_2(\omega)$ originates from interband electronic transitions, $\sigma(\omega)$ describes the generation of photoexcited charge carriers under incident electromagnetic radiation [46]. The calculated $\sigma(\omega)$ spectra show that the electrical conductivity is nearly zero at low photon energies and increases progressively with increasing energy, confirming the semiconducting character of MoX_2 compounds. The main conductivity peaks arise from electronic transitions between the valence and conduction bands, while the enhanced conductivity in the visible and near-infrared regions suggests the suitability of these layered materials for photoelectronic and photoconductive applications. A strong optical conductivity peak is observed for the MoX_2 compounds in the visible region, between 1.0 and 2.50 eV, indicating efficient interband electronic transitions and charge-carrier generation under light irradiation. The optical conductivity increases near the absorption edge, with maximum peaks of approximately 11269, 9112, and 8495 $1/\Omega$cm, and decreases gradually at higher photon energies, consistent with the semiconducting nature and indicating favorable optical characteristics for potential optoelectronic applications.

The real and imaginary parts of the dielectric function, $\varepsilon_1(\omega)$ and $\varepsilon_2(\omega)$, were used to evaluate the absorption coefficient $\alpha(\omega)$ and the optical conductivity $\sigma(\omega)$ [49,50]. This $\alpha(\omega)$ coefficient is given by: $\alpha(\omega) = \sqrt{2\omega}\left(\sqrt{\varepsilon_1^2(\omega) + \varepsilon_2^2(\omega)} - \varepsilon_1(\omega)\right)^{1/2}$. Calculated absorption spectra $\alpha(\omega)$ of MoX_2 (X = S, Se, Te) in Figure 7(d) reveal strong absorption extending from visible to ultraviolet regions, mainly due to interband electronic transitions. The maximum absorption $\alpha_{max}(\omega)$ values at low and high energies are summarized in Table 2. The absorption edge shifts towards lower energies from MoS_2 to $MoTe_2$ due to the reduction in band gap with increasing chalcogen atomic size. The pronounced visible–UV absorption and enhanced optical response indicate that these layered compounds are promising candidates for photovoltaic, solar-energy systems, and photoelectronic applications.

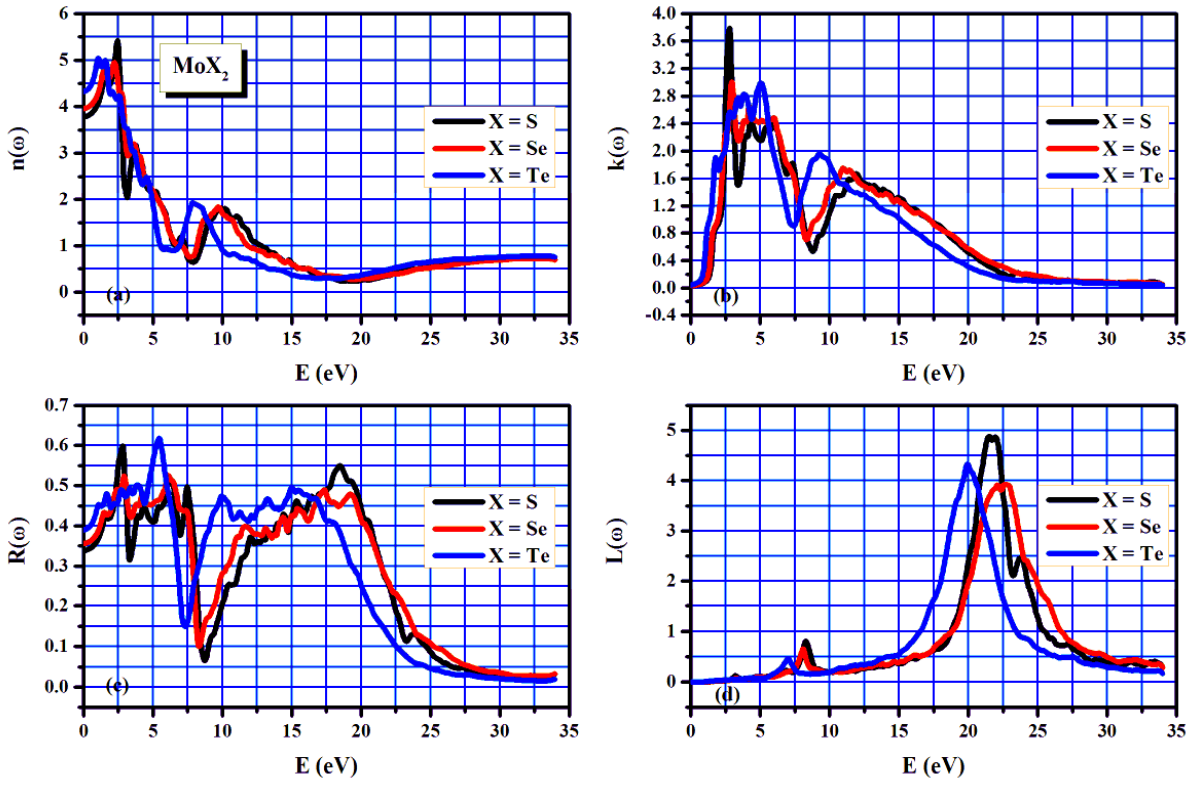


Figures 7. The calculated spectra of (a) real part $\varepsilon_1(\omega)$, (b) imaginary part $\varepsilon_2(\omega)$, (c) optical conductivity $\sigma(\omega)$, and (d) absorption coefficient $\alpha(\omega)$ for MoX_2 (X = S, Se, Te) monolayers using the GGA-mBJ approach.

Moreover, the refractive index $n(\omega)$, extinction coefficient $k(\omega)$, reflectivity $R(\omega)$, and energy-loss function $L(\omega)$ of the investigated MoX_2 (X = S, Se, Te) compounds were calculated and plotted in Figure 8. The refractive index $n(\omega)$ was calculated from the real and imaginary parts of the dielectric function: $n(\omega) = \frac{1}{\sqrt{2}}\left(\sqrt{\varepsilon_1^2(\omega) + \varepsilon_2^2(\omega)} + \varepsilon_1(\omega)\right)^{1/2}$ [50]. Figure 8(a) shows that the obtained $n(\omega)$ spectra follow the same trend as the real dielectric constant $\varepsilon_1(\omega)$. As shown in Table 2, the static refractive index $n(0)$ satisfies the relation $n(0) = \sqrt{\varepsilon_1(0)}$ [50]. The refractive index $n(\omega)$ increases with photon energy, reaches maximum values in the visible region, 1–2 eV, and then decreases gradually at higher energies. This variation from MoS_2 to $MoTe_2$ is mainly associated with changes in band gap and electronic polarizability. The relatively large $n(\omega)$ values indicate strong interaction between electromagnetic radiation and the layered MoX_2 structures, supporting their potential for photonic and optoelectronic applications.

The extinction coefficient $k(\omega)$ in Figure 8(b), which describes the attenuation of electromagnetic waves inside the MoX_2 materials due to optical absorption, was calculated using: $k(\omega) = \frac{1}{\sqrt{2}}\left(\sqrt{\varepsilon_1^2(\omega) + \varepsilon_2^2(\omega)} - \varepsilon_1(\omega)\right)^{1/2}$ [49,50]. The calculated $k(\omega)$ spectra increase with photon energy, reach prominent peaks in the visible-UV region, 3.829 at 2.76 eV, 3.054 at

3.00 eV, and 3.053 at 4.93 eV, for MoX_2, respectively. Then $k(\omega)$ decreases gradually at higher energies. The strong peaks indicate enhanced interband electronic transitions and efficient light absorption in the MoX_2 compounds, whereas the smaller $k(\omega)$ values at low energies correspond to higher potential transparency. The optical constants are related to the dielectric function through: $\varepsilon_1(\omega) = n^2(\omega) - k^2(\omega)$ and $\varepsilon_2(\omega) = 2n(\omega)k(\omega)$ [32,50]. These relations demonstrate the strong correlation between the dielectric response and the optical behavior of the layered MoX_2 materials.



Figures 8. GGA-mBJ calculation spectra of (a) refractive index $n(\omega)$, (b) extinction coefficient $k(\omega)$, (c) reflectivity $R(\omega)$, and (d) energy-loss function $L(\omega)$ for MoX_2 (X = S, Se, Te) monolayers.

The optical reflectively $R(\omega)$ of the MoX_2 (X = S, Se, Te) compounds was determined from the dielectric function using: $R(\omega) = \left(\frac{\sqrt{\varepsilon(\omega)}-1}{\sqrt{\varepsilon(\omega)}+1}\right)^2$. Reflectively describes the fraction of incident electromagnetic radiation reflected from the material surface and is strongly influenced by interband electronic transitions. The calculated $R(\omega)$ spectra in Figure 8(c) show reflectively in the visible region, indicating efficient light absorption in the MoX_2 materials. The reflectively reaches its maximum in the visible-UV energy range and then decreases gradually at higher photon energies. These results are consistent with the high absorption coefficient and optical conductivity, confirming the suitability of layered MoX_2 materials for photovoltaic and optoelectronic applications. The reflectively $R(\omega)$ can be expressed in terms of the refractive

index $n(\omega)$ and extinction coefficient $k(\omega)$ as: $R(\omega) = \frac{(n(\omega)-1)^2+k^2(\omega)}{(n(\omega)+1)^2+k^2(\omega)}$ [47,48]. In the static limit, 0 eV, where $k(0) = 0$, the reflectively depends mainly on the static refractive index $n(0)$. The obtained static reflectivity $R(0)$, 0.340, 0.361, and 0.394, are consistent with those extracted directly from the calculated $R(\omega)$ spectra, 0.337, 0.361, and 0.395, respectively, see Table 2, confirming the reliability of the optical analysis for the MoX_2 (X = S, Se, Te) compounds.

Among the calculated optical parameters, the energy-loss function $L(\omega)$ is particularly important because it describes the energy loss of fast-moving electrons inside the MoX_2 (X = S, Se, Te) compounds. When incident photons interact with the crystal surface, electrons undergo scattering processes that lead to energy dissipation. The calculated $L(\omega)$ spectra in Figure 8(d) start from nearly zero and then increase to pronounced peaks in the high-energy region, corresponding to plasma resonances. MoX_2 compounds show maximum $L(\omega)$ of 4.916 at 21.5 eV, 3.991 at 22.5 eV, and 4.387 at 20 eV. These peaks are associated with plasma frequency (ω_p), which can be determined from: $E_p = \hbar\omega_p$ [48,51]. The plasma frequency reflects the collective oscillation of charge carriers and provides valuable insight into the electronic response and optical behavior of the layered MoX_2 materials.

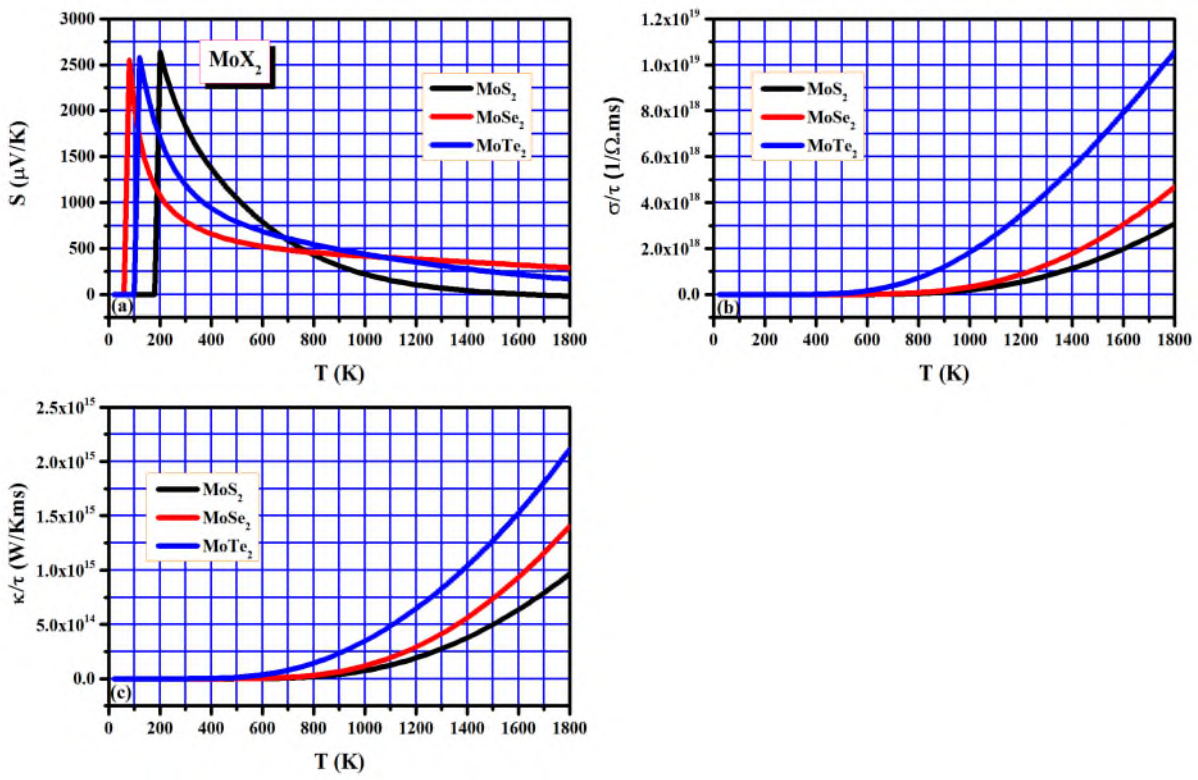
3.4. Thermoelectronic properties

2D materials, including atomically thin TMCs, VI-based chalcogenides, and other layered van der Waals systems, exhibit unique electrical and thermal characteristics that differ significantly from those of their bulk forms [2,52]. Owing to their reduced dimensionality, these materials often display an enhanced Seebeck coefficient as a result of quantum confinement effects, while their lattice thermal conductivity is markedly lowered by strong phonon scattering and interface-induced thermal resistance [53]. In addition, their anisotropic crystal structures and tunable electronic band gaps provide effective control over carrier transport and heat conduction, leading to improved thermoelectronic efficiency and higher thermoelectronic figure of merit (ZT) values [2,54]. Several strategies have been widely employed to regulate electrical and thermal transport properties of these 2D materials, thereby enhancing overall thermoelectronic performance [55]. Furthermore, recent progress in interfaces modeling and engineering and 2D heterostructures has enhanced the development of lightweight and flexible thermoelectronic devices for applications in waste-heat harvesting, microelectronic cooling, and wearable energy systems [56]. These advances highlight the important role of 2D materials in sustainable energy technologies, thermal management, and decentralized power generation from low-temperature heat sources [2,24,41,44,54].

Based on the electronic semiconducting of these monolayers MoX_2 (X = S, Se, Te), we calculated the thermoelectronic and transport properties using the BoltzTraP software [33]. In this study, we use the relaxation time approximation with ($\tau = 1.0\times10^{-14}$ s) to solve the semi-classical Boltzmann transport equation. Figure 9 shows the plots of Seebeck coefficient (S), electrical conductivity (σ/τ), power factor ($S^2\sigma/\tau$), thermal conductivity (κ/τ), figure of merit (ZT), and heat capacity (C_V), computed as a function of temperature (T) over the range from $T = 0$ K to $T = 1800$ K. It is clear that these transport coefficients exhibit a similar trend as T increasing, which are in good agreement with previous theoretical studies [57-59]. The S coefficient (Figure 9(a)) starts from zero and increases rapidly with T to reach it maximum value (S_{max}) at low T, of about 2.646 V/T (at $T = 200$ K) for MoS_2, 2.551 V/T (at $T = 80$ K) for $MoSe_2$, and 2.578 V/T (at $T = 120$ K) for $MoTe_2$. After the reaching peak, S decreases gradually as T continuous to increase. It shows 1.830, 0.797, and 1.191 V/T at room temperature ($T = 300$ K), which decrease to 0.312, 0.437, and 0.490 V/T, respectively, at higher temperatures such as ($T = 900$ K). Accordingly, the present calculations reveal that MoS_2 has the highest S coefficient at 300 K among this series. The S coefficient, which measures the voltage generated as a result of the T gradient $S = -\Delta V/\Delta T$, is a vital transport quantity used to evaluate the thermoelectric performance. Large S values indicate strong ability to convert thermal energy into electrical energy. The calculated S coefficient for MoX_2 structures agrees well with the previously reported results [57,59].

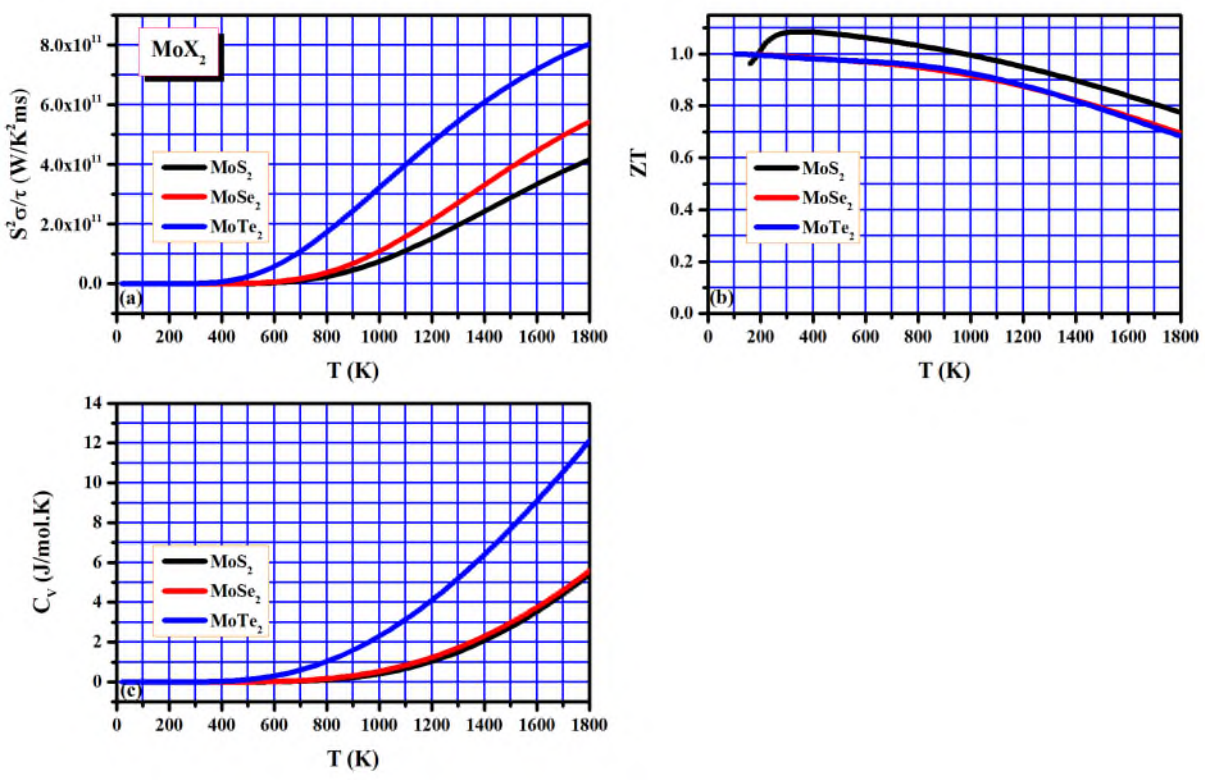
Figures 9(b) and 9(c) display the T-dependent electrical σ/τ and thermal κ/τ conductivities per relaxation time for MoX_2, which show similar behavior with T. At ($T = 300$ K), the calculated σ/τ values are about 4.872×10^{11} $1/\Omega ms$ (MoS_2), 2.265×10^{12} $1/\Omega ms$ ($MoSe_2$), and 7.396×10^{14} $1/\Omega ms$ ($MoTe_2$). At higher temperatures ($T = 900$ K), these values rise significantly to 1.026×10^{17}, 1.785×10^{17}, and 1.214×10^{18} $1/\Omega ms$, respectively. The observed increase in σ/τ at elevated T is related to relatively narrow band-gap E_g of these 2D structures, which reduces carrier freeze-out and increases the carrier concentration n as T rises. The results of T-dependent κ/τ per relaxation time, shown in Figure 9(c), originate from the transport of electronic charge carriers through the material. All three 2D compounds exhibit very similar behavior with increasing T, where, it is zero at ($T = 300$ K), and then increases rapidly as T rises. At ($T = 300$ K), the calculated κ/τ values are approximately 3.837×10^{8} W/mKs for MoS_2, 1.446×10^{9} W/mKs for $MoSe_2$, and 2.168×10^{11} W/mKs for $MoTe_2$. These results indicate that the minimum κ/τ occurs near room temperature, which coincides with the region where the S coefficient reaches its maximum value. This correlation supports the strong thermoelectronic performance of the our 2D systems. At higher temperatures, such as ($T = 900$ K), κ/τ increases

significantly, reaching about 4.077×10^{13}, 6.547×10^{13}, and 2.336×10^{14} W/mKs, respectively. Among these 2D-MoX_2 materials, $MoTe_2$ shows the largest κ/τ at elevated temperatures. Moreover, due to its narrow electronic band-gap (0.860 eV), the $MoTe_2$ shows highest electrical σ/τ and thermal κ/τ conductivities compared to $MoSe_2$ and MoS_2. Our results indicate that the electronic contribution of thermal conductivity κ/τ in all these monolayers MoX_2 (X = S, Se, Te) exhibits similar behavior as for the electrical conductivity σ/τ. This implies that the 2D systems satisfy the Wiedemann-Franz, which states that the ratio of κ/τ to σ/τ is directly proportional to their absolute T ($\frac{\kappa}{\sigma} = LT$; the Lorenz Number $L = \left(\pi k_B/\sqrt{3}e\right)^2 \approx 2.44\times10^{-8}\ W\Omega/T^2$) [57].



Figures 9. (a) Seebeck coefficient (S), (b) electrical conductivity (σ/τ), and (c) thermal conductivity (κ/τ) as a function of temperature (T) for MoX_2 (X = S, Se, Te) monolayers.

The results of thermoelectronic power factor ($S^2\sigma/\tau$) signify the ability of MoX_2 materials to convert heat into electrical energy; therefore, evaluate the thermoelectric efficiency. This parameter depends on electrical conductivity σ/τ and Seebeck coefficient S. In all systems, it starts from zero at ($T = 0$ K) and increases as the T rises (see Figure 10(a)). At ($T = 300$ K), MoX_2 show $S^2\sigma/\tau$ of about 1.386×10^{6}, 4.773×10^{6}, and 7.141×10^{7} W/K^2ms, respectively, which increase to approximately 4.597×10^{10} W/K^2ms for MoS_2, 6.802×10^{10} W/K^2ms for $MoSe_2$, and 2.448×10^{11} W/K^2ms for $MoTe_2$ at higher temperatures ($T = 900$ K). The obtained values indicates that 2D materials possess promising transport features suitable for advanced thermoelectronic devices.



Figures 10. (a) Power factor ($S^2\sigma/\tau$), (b) figure of merit (ZT), and (c) heat capacity (C_V), as a function of temperature (T) for MoX_2 (X = S, Se, Te) monolayers.

Furthermore, the overall thermoelectronic efficient of MoX_2 is usually evaluated using the dimensionless figure of merit ZT. It depends mainly on electrical conductivity σ, Seebeck coefficient S is the, thermal conductivity κ, and absolute temperature T ($ZT = \sigma S^2 T/\kappa$) [60]. The ZT plots in (Figure 10(b)) show that parameter starts greater than unity at low temperatures and vary with increasing T. At ($T = 300$ K), the highest value is obtained for MoX_2 with $ZT \approx 1.083$ (MoS_2), $ZT \approx 0.991$ ($MoSe_2$), and $ZT \approx 0.988$ ($MoTe_2$). The higher ZT value of MoS_2 monolayer is mainly due to its lower thermal conductivity κ, consistent with the inverse dependence of ZT on κ. At higher temperatures ($T = 900$ K), these ZT values gradually decrease, reaching approximately 1.015 for (X = S), 0.935 for (X = Se), and 0.943 for (X = Te). The higher thermoelectronic figure of merit shown by MoS_2 among the other two systems confirm the observed trend for both S and $S^2\sigma/\tau$ parameters. Also, despite having the lowest S, its high σ and low κ help to enhance this ZT. The variation of molar specific heat capacity at constant volume C_V with the T for the studied 2D materials (Figure 10(c)) was calculated from the change in internal energy via ($C_V = \Delta U/n\Delta T$). At low temperatures ($T = 300$ K), C_V remains very small, approximately zero, and then increases rapidly to 0.226 $J/mol.K$ (MoS_2), 0.314 $J/mol.K$ ($MoSe_2$), and 1.596 $J/mol.K$ ($MoTe_2$) at ($T = 900$ K). These values indicate that the studied 2D materials can absorb significant thermal energy over a wide T range, which supports their potential use in thermoelectronic applications.

4. Conclusion

First-principles density functional theory (DFT) calculations were performed to systematically investigate the structural, optoelectronic, and thermoelectronic properties of the 2D transition-metal dichalcogenides (TMDs) MoX_2 (X = S, Se, Te). The simulations, carried out using the FP-LAPW approach within the Wien2k package, confirm the structural stability of these 2D-MoX_2 compounds. The results of optimized structures and formation energies confirm that all bulk MoX_2 compounds are thermodynamically stable in the hexagonal symmetry with $P6_3/mmc$ phase. Electronic structure calculations using the generalized gradient approximation (GGA) and GGA-modified Becke–Johnson (GGA-mBJ) potential reveal that MoX_2 monolayers exhibit semiconducting behavior with narrow band-gaps E_g. The calculated direct band-gap ranges are 1.196–1.295 eV for MoS_2, 1.030–1.235 eV for $MoSe_2$, and 0.930–1.039 eV for $MoTe_2$. The GGA-mBJ calculations provide improved direct band gaps estimates and improved the description of optoelectronic properties. The obtained band-gap values indicate strong absorption in the visible region, highlighting the suitability of these 2D-MoX_2 materials for photoelectronic applications. The optical parameters analysis, including dielectric function, absorption coefficient, optical conductivity, refractive index, reflectivity, and energy-loss function, shows strong optical absorption and significant photoresponse in the visible–ultraviolet region, indicating their promising optoelectronic for solar-energy, photovoltaic, and photodetection applications. Thermoelectric parameters of MoX_2 compounds, evaluated using the BoltzTraP package, demonstrate a clear dependence on the X-site, which strongly affects the charge-carrier transport and thermoelectronic efficiency. The investigated monolayers MoX_2 exhibit low thermal conductivity and enhanced electrical transport properties, leading to favorable thermoelectronic figure of merit of about $ZT = 1.083$, 0.991, and 0.988 for MoS_2, $MoSe_2$, and $MoTe_2$, respectively, under the adopted computational conditions. Overall, the present first-principles DFT calculations indicate that the 2D-MoX_2 compounds possess interesting direct band-gap semiconducting, optoelectronic, and thermoelectric properties. These characteristics suggest potential for future photoelectronic, thermoelectronic, and energy-conversion technologies. Further experimental investigations are required to validate the calculated properties and assess the practical applicability of these materials.

Author Contributions

All authors wrote the main manuscript text. **M.M.** and **B.O.** computed the physical properties. **M.M.** and **A.A.** plotted all figures and prepared Tables. All authors reviewed the manuscript.

Data Availability

The datasets used and/or analyzed during this study are available from the corresponding authors upon reasonable request

Acknowledgments

The Researchers would like to thank the Deanship of Graduate Studies and Scientific Research at Qassim University (www.qu.edu.sa) for financial support (QU-APC-2026)

References

[1] K.S. Novoselov, A.K. Geim, S.V. Morozov, D. Jiang, Y. Zhang, S.V. Dubonos, I.V. Grigorieva, and A.A. Firsov, Electric Field Effect in Atomically Thin Carbon Films, Science 306 (5696), (2004), 666. https://doi.org/10.1126/science.1102896

[2] A.K. Geim and I.V. Grigorieva, Van der Waals Heterostructures, Nature 499 (7459), (2013), 419–425. https://doi.org/10.1038/nature12385

[3] S.Z. Butler, S.M. Hollen, L. Cao, Y. Cui, J.A. Gupta, H.R. Gutiérrez, T.F. Heinz, S.S. Hong, J. Huang, A.F. Ismach, E. Johnston-Halperin, M. Kuno, V.V. Plashnitsa, R.D. Robinson, R.S. Ruoff, S. Salahuddin, J. Shan, L. Shi, M.G. Spencer, M. Terrones, W. Windl, and J.E. Goldberger, Progress, Challenges, and Opportunities in Two-Dimensional Materials Beyond Graphene, ACS Nano 7 (4), (2013), 2898–2926. https://doi.org/10.1021/nn400280c

[4] N.R. Abdullah, B.J. Abdullah, B.R. Pirot, and V. Gudmundsson, Comprehensive Investigation of Structural, Electronic, Thermal, and Optical Properties of 2D Hexagonal LaN: Insights from DFT and AIMD Simulations with HSE06 Functional, Materials Science in Semiconductor Processing 199 (2025), 109836. https://doi.org/10.1016/j.mssp.2025.109836

[5] Z. Gao, M.-Q. Zhao, M.M.A. Ashik, and A.T.C. Johnson Jr., Recent Advances in the Properties and Synthesis of Bilayer Graphene and Transition Metal Dichalcogenides, Journal of Physics: Materials 3 (2020), 042003. https://doi.org/10.1088/2515-7639/abb58d

[6] L. Vogt, P. De Padova, C. Quaresima, J. Avila, E. Frantzeskakis, M.C. Asensio, A. Resta, B. Ealet, and G. Le Lay, Silicene: Compelling Experimental Evidence for Graphene-Like Two-Dimensional Silicon, Physical Review Letters 108 (15), (2012), 155501. https://doi.org/10.1103/PhysRevLett.108.155501

[7] L. Li, Y. Yu, G.J. Ye, Q. Ge, X. Ou, H. Wu, D. Feng, X.H. Chen, and Y. Zhang, Black Phosphorus Field-Effect Transistors, Nature Nanotechnology 9 (5), (2014), 372–377. https://doi.org/10.1038/nnano.2014.35

[8] S. Zhang, Z. Yan, Y. Li, Z. Chen, and H. Zeng, Atomically Thin Arsenene and Antimonene: Semimetal–Semiconductor and Indirect–Direct Band-Gap Transitions, Angewandte Chemie International Edition 54 (10), (2015), 3112–3115. https://doi.org/10.1002/anie.201411246

[9] M. Chhowalla, H.S. Shin, G. Eda, L.J. Li, K.P. Loh, and H. Zhang, The Chemistry of Two-Dimensional Layered Transition Metal Dichalcogenide Nanosheets, Nature Chemistry 5 (4), (2013), 263–275. https://doi.org/10.1038/nchem.1589

[10] Q.H. Wang, K. Kalantar-Zadeh, A. Kis, J.N. Coleman, and M.S. Strano, Electronics and Optoelectronics of Two-Dimensional Transition Metal Dichalcogenides, Nature Nanotechnology 7 (11), (2012), 699–712. https://doi.org/10.1038/nnano.2012.193

[11] A. Splendiani, L. Sun, Y. Zhang, T. Li, J. Kim, C.Y. Chim, G. Galli, and F. Wang, Emerging Photoluminescence in Monolayer MoS_2, Nano Letters 10 (4), (2010), 1271–1275. https://doi.org/10.1021/nl903868w

[12] A. Kuc, N. Zibouche, and T. Heine, Influence of Quantum Confinement on the Electronic Structure of the Transition Metal Sulfide TS_2, Physical Review B 83 (24), (2011), 245213. https://doi.org/10.1103/PhysRevB.83.245213

[13] S. Hasan, M.T. Ahmed, A.A. Roman, S. Islam, and F. Ahmed, Investigation of Structural, Electronic, and Optical Properties of Chalcogen-Doped ZrS_2: A DFT Analysis, Advances in Materials Science and Engineering 2023 (2023), Article ID 6525507. https://doi.org/10.1155/2023/6525507

[14] S.A. Yamusa, A. Shaari, N.A.M. Alsaif, I.M. Alsalamah, I. Isah, and N. Rekik, First-Principles Investigation of Structural, Electronic, and Optical Properties of 2D Transition Metal Dichalcogenides, ACS Omega 7 (49) (2022), 45719–45731. https://doi.org/10.1021/acsomega.2c07030

[15] C.R. Dean, A.F. Young, I. Meric, C. Lee, L. Wang, S. Sorgenfrei, K. Watanabe, T. Taniguchi, P. Kim, K.L. Shepard, and J. Hone, Boron Nitride Substrates for High-Quality Graphene Electronics, Nature Nanotechnology 5 (10), (2010), 722–726. https://doi.org/10.1038/nnano.2010.172

[16] M. Naguib, M.W. Barsoum, Y. Gogotsi, V. Presser, P.L. Taberna, and P. Simon, Two-Dimensional Nanocrystals Produced by Exfoliation of Ti_3AlC_2, Advanced Materials 23 (37), (2011), 4248–4253. https://doi.org/10.1002/adma.201102306

[17] A. Ambrosi, Z. Sofer, and M. Pumera, 2D Materials beyond Graphene and Transition Metal Dichalcogenides, Chemical Society Reviews 45 (10), (2016), 2740–2755. https://doi.org/10.1039/C5CS00715C

[18] S. Manzeli, D. Ovchinnikov, D. Pasquier, O.V. Yazyev, and A. Kis, 2D Transition Metal Dichalcogenides, Nature Reviews Materials 2 (8), (2017), 17033. https://doi.org/10.1038/natrevmats.2017.33

[19] R. Lv, Q. Li, A.R. Botello-Méndez, T. Hayashi, B. Wang, A. Berkdemir, Q. Hao, A.L. Elias, R. Cruz-Silva, H.R. Gutiérrez, N. Perea-López, A.L. Elías, H. Terrones, M. Terrones, M.S. Dresselhaus, and T. Endo, Two-

Dimensional Transition Metal Dichalcogenides: Clusters, Ribbons, Sheets and More, Nano Today 10 (5) (2015), 559–592. https://doi.org/10.1016/j.nantod.2015.06.004

[20] T.F. Heinz and K.F. Mak, The Evolution of Electronic Structure in Atomically Thin Transition-Metal Dichalcogenides, Nature Photonics 10 (4), (2016), 216–226. https://doi.org/10.1038/nphoton.2016.36

[21] M. Voiry, A. Mohite, and M. Chhowalla, Phase Engineering of Transition Metal Dichalcogenides, Chemical Society Reviews 44 (9), (2015), 2702–2712. https://doi.org/10.1039/C5CS00151J

[22] H. Habib, W. Zhao, S. Mir, L. Ma, and G. Tian, First-Principles Studies on the Structural, Electronic, and Optical Properties of 2D Transition Metal Dichalcogenide and Janus TMDC Heterobilayers, Journal of Physics: Condensed Matter 35 (2023), 505501. https://doi.org/10.1088/1361-648X/acf987

[23] Y. Zhao, J. Qiao, P. Yu, Z. Hu, Z. Lin, S.P. Lau, Z. Liu, W. Ji, and Y. Chai, High-Electron-Mobility and Air-Stable 2D Layered $PtSe_2$ FETs, Nano Letters 17 (6), (2017), 3478. https://doi.org/10.1021/acs.nanolett.7b00049

[24] C. Yim, K. Lee, N. McEvoy, M. O'Brien, S. Riazimehr, F. Berner, C. Cullen, J. Kotakoski, C. Meyer, M. Ghorbani-Asl, S. Krishnamurthy, B.C. Bayer, A. Kaestner, S. Szabó, E. Rezvani, A. Kulkarni, A. Böttger, J. Nagle, and G.S. Duesberg, High-Performance Hybrid Electronic Devices from Layered $PtSe_2$ Films Grown at Low Temperature, ACS Nano 8 (5), (2014), 4779–4787. https://doi.org/10.1021/nn501138k

[25] X. Zhou, H. Sun, and X. Bai, Two-Dimensional Transition Metal Dichalcogenides: Synthesis, Biomedical Applications and Biosafety Evaluation, Frontiers in Bioengineering and Biotechnology 8 (2020), 236. https://doi.org/10.3389/fbioe.2020.00236

[26] R.A. Ghazi, D.A. Sabur, R.S. Al-Hasnawy, H.O. Muhsen, B.B. Kadhim, F.M. Salim, H.R. Jappor, and A.M. Ali, Structural, Electronic and Optical Properties of Transition Metal Dichalcogenide Layers PtS_2 and $PtSe_2$ for Nano-Device Applications, Key Engineering Materials 886 (2021), 48–56. https://doi.org/10.4028/www.scientific.net/KEM.886.48

[27] P. Blaha, K. Schwarz, P. Sorantin, and S. B. Trickey, Full-potential, linearized augmented plane wave programs for crystalline systems, Comput. Phys. Commun. 59, (1990), 399-415. https://doi.org/10.1016/0010-4655(90)90187-6

[28] K. H. Schwarz, P. Blaha, and G. K. H. Madsen, Electronic structure calculations of solids using the WIEN2k package for material sciences, Comput. Phys. Commun. 147 (2002) 71-76. https://doi.org/10.1016/S0010-4655(02)00206-0

[29] W. Kohn, and L.J. Sham, Self-Consistent Equations Including Exchange and Correlation Effects, Phys. Rev. 140 A, (1965), 1133. https://doi.org/10.1103/PhysRev.140.A1133

[30] J. P. Perdew, K. Burke, and M. Ernzerhof, Generalized gradient approximation made simple, Phys. Rev. Lett. 77, (1996), 3865. https://doi.org/10.1103/PhysRevLett.77.3865

[31] D. Koller, F. Tran, and P. Blaha, Improving the modified Becke-Johnson exchange potential, Phys. Rev. B 85, (2012), 155109. https://doi.org/10.1103/PhysRevB.85.155109

[32] M. Musa Saad H.-E., B.O. Alsobhi, and A. Almeshal, A Systematic Study of the Structural, Electronic and Optical Properties of 3d, 4d and 5d Binary Transition Metal Arsenides $TMAs_2$ (TM = Fe, Ru, Os). Braz. J. Phys. 55, 146 (2025). https://doi.org/10.1007/s13538-025-01782-1

[33] G.K.H. Madsen, and D.J. Singh, BoltzTraP. A code for calculating band-structure dependent quantities, Comput. Phys. Commun. 175, (2006), 67-7. https://doi.org/10.1016/j.cpc.2006.03.007

[34] F.D. Murnaghan, The Compressibility of Media under Extreme Pressures, PNAS 30(9), (1944), 244. https://doi.org/10.1073/pnas.30.9.244

[35] B. Schönfeld, J.J. Huang, S.C. Moss, Anisotropic mean-square displacements (MSD) in single-crystals of 2H- and 3R-MoS_2, Acta Cryst. B. 39 (4), (1983), 404. https://doi.org/10.1107/S0108768183002645

[36] L.A.H. Jones, Z. Xing, J.E.N. Swallow, H. Shiel, T.J. Featherstone, M.J. Smiles, N. Fleck, P.K. Thakur, T.-L. Lee, L.J. Hardwick, D.O. Scanlon, A. Regoutz, T.D. Veal, and V.R. Dhanak, Band Alignments, Electronic Structure, and Core-Level Spectra of Bulk Molybdenum Dichalcogenides (MoS_2, $MoSe_2$, and $MoTe_2$), J. Phys. Chem. C 126, (2022), 21022. https://doi.org/10.1021/acs.jpcc.2c05100

[37] M.K. Agarwal, P.D. Patel, and R.M. Joshi, Growth conditions and structural characterization of $MoSe_xTe_{2-x}$ ($0 \leqslant x \leqslant 2$) single crystals, J. Mater. Sci. Lett. 5, (1986), 66. https://doi.org/10.1007/BF01671439. S2CID 96858586

[38] R. Sankar, G.N. Rao, I. Panneer Muthuselvam, C. Butler, N. Kumar, G. Senthil Murugan, C. Shekhar, T.-R. Chang, C.-Y. Wen, C.-W. Chen, W.-L. Lee, M.-T. Lin, H.-T. Jeng, C. Felser, and F. C. Chou, Polymorphic Layered $MoTe_2$ from Semiconductor, Topological Insulator, to Weyl Semimetal, Chem. Mater. 29 (2) (2017) 699. https://doi.org/10.1021/acs.chemmater.6b04363

[39] N. Nagappan a 1, G. Sudha Priyanga a b 1, Tiju Thomas, Prediction of crystal structure, phase group, and stability of 2D materials through data science coupled with DFT, Physica B: Condensed Matter 696, (2025), 416638. https://doi.org/10.1016/j.physb.2024.416638

[40] S. Manzeli, D. Ovchinnikov, D. Pasquier, O.V. Yazyev, and A. Kis, 2D transition metal dichalcogenides. Nat. Rev. Mater. 2, (2017), 17033. https://doi.org/10.1038/natrevmats.2017.33

[41] S. Berri, and N. Bouarissa, Electronic structure and fundamental properties of MoX_2 (X=Te, Se and S) compound materials at high pressures and elevated temperatures, Comput. Condens. Matter 28, (2021), e00574. https://doi.org/10.1016/j.cocom.2021.e00574

[42] D.M. Guzman, A. Strachan, Role of strain on electronic and mechanical response of semiconducting transition-metal dichalcogenide monolayers: An ab-initio study, J. Appl. Phys. 115, (2014), 243701. https://doi.org/10.1063/1.4883995

[43] T. Boker, R. Severin, A. Muller, C. Janowitz, R. Manzke, D. Voss, P. Kruger, A. Mazur, and J. Pollmann, Band structure of MoS2, MoSe2, and $\alpha-$MoTe2 : Angle-resolved photoelectron spectroscopy and ab initio calculations, Phys. Rev. B 64, (2001), 235305. https://doi.org/10.1103/PhysRevB.64.235305

[44] S.J. Zelewski, and R. Kudrawiec, Photoacoustic and modulated reflectance studies of indirect and direct band gap in van der Waals crystals, Sci. Rep. 7, (2017), 15365. https://doi.org/10.1038/s41598-017-15763-1

[45] A. Almeshal, M. Musa Saad H.-E., and B.O. Alsobhi, A comprehensive study of physical properties of TMP_2 (TM = Fe, Ru, Os): As semiconductors for optoelectronic and thermoelectronic applications, Results Phys. 72, (2025), 10821. https://doi.org/10.1016/j.rinp.2025.108211

[46] M. Musa Saad H.-E., and B. O. Alsobhi, Mechanical, optoelectronic and thermoelectronic properties of double perovskites halides Rb_2TCl_6 [T = V, Cr, Mn] for optoelectronics and thermoelectronic applications, J. Phys. Chem. Solids 194, (2024), 112246. https://doi.org/10.1016/j.jpcs.2024.112246

[47] H. A. Alburaih, W. Tanveer, N. A. Noor, F. Ali, H. Riaz, A. Laref, and M. M. Saad H.-E., Opto-electronic and thermoelectric properties of double perovskites Li_2CuGaX_6 (X = Cl, Br, I) for energy conversion applications: DFT calculations, J. Mater. Res. 39, (2024), 1207. https://doi.org/10.1557/s43578-024-01303-x

[48] W. A. C. P. Wanniarachchi, H. Eidsvåg, T. Arunasalam, P. Ravirajan, D. Velauthapillai, and P. Vajeeston, Deep insight into structural and optoelectronic properties of mixed anion perovskites, Mater. Res. Express 11, (2024), 025901. https://doi.org/10.1088/2053-1591/ad1f98

[49] T. S. Ahmad, N. Ehsan, M. Liaqat, S. M. S. Gilani, A. U. Haq, A. M. Quraishi, D. Abduvalieva, V. Tirth, A. Algahtani, R. M. Mohammed, N. M. A. Hadia, A. M. Alsuhaibani, M. S. Refat, A. Zaman, Optoelectronic and thermoelectric analysis of halide stable double perovskite Rb_2TlSbX_6 (X = Cl, Br, I) via DFT calculations, Results Phys. 63, (2024), 107885. https://doi.org/10.1016/j.rinp.2024.107885

[50] M. M. Saad H.-E., and B. O. Alsobhi, Optoelectronic and thermoelectronic properties of 3d, 4d, and 5d based semiconductor half-Heuslers (Ni/Pd/Pt)ScSb with narrow bandgap, Comput. Condens. Matter 36, (2023), e00831. https://doi.org/10.1016/j.cocom.2023.e00831

[51] M.A.S. Alothoum, S.A. Yamusa, and N. Rekik, DFT Study on the Impact of Cr, Ta, and Mn Doping in Monolayer MoS_2 for Photodetection Applications. J. Electron. Mater. 54, (2025), 8979. https://doi.org/10.1007/s11664-025-12110-3

[52] K.F. Mak, C. Lee, J. Hone, J. Shan, and T.F. Heinz, Atomically Thin MoS_2: A New Direct-Gap Semiconductor, Phys. Rev. B 105, (2010), 136805. https://doi.org/10.1103/PhysRevLett.105.136805

[53] H. Li, Q. Zhang, C.C.R. Yap, B.K. Tay, T.H.T. Edwin, A. Olivier, and D. Baillargeat, From Bulk to Monolayer MoS2: Evolution of Raman Scattering, Advanced Functional Materials 22 (7), (2012), 1385. https://doi.org/10.1002/adfm.201102111

[54] A. Patel, D. Singh, Y. Sonvane, P.B. Thakor, and R. Ahuj, High Thermoelectric Performance in Two Dimensional Janus Monolayer Material WS-X (X = Se and Te), ACS Appl. Mater. Interfaces 12 (41), (2020), 46212. https://doi.org/10.1021/acsami.0c13960

[55] Z.-M. Zhang, W.-L. Chang, Z.-Q. Sun, X.-H. He, J.-L. Zhang, X.-P. Wei, and X. Tao, Thermoelectric properties of two-dimensional ternary transition metal nitrides HfNF, Int. J. Quantum Chem. 124 (3), (2024), e27350. https://doi.org/10.1002/qua.27350

[56] G.-h. Xiong, T. Liu, H.-h. Huang, and J. Wang, Thermoelectric properties of Janus BiXI

(X = S and Se) monolayers: A first-principles study, J. Appl. Phys. 136, (2024), 185102. https://doi.org/10.1063/5.0221109

[57] M. Buscema, M. Barkelid, V. Zwiller, H.S.J. van der Zant, G.A. Steele, and A. C.-Gomez, Large and Tunable Photothermoelectric Effect in Single-Layer MoS_2, Nano Lett. 13, (2013), 358. https://doi.org/10.1021/nl303321g

[58] G. Zhang, and Y.-W. Zhang, Thermoelectric properties of two-dimensional transition metal dichalcogenides, J. Mater. Chem. C 5, (2017), 7684. https://doi.org/10.1039/C7TC01088E

[59] R. Wisesa, A. Azhar, and E. Suprayoga, Thermal transport and thermoelectric properties of transition metal dichalcogenides MoX_2 from first-principles calculation, Phys. Scr. 99, (2024), 035929. https://doi.org/10.1088/1402-4896/ad25b8

[60] X.-P. Wei, J. Shen, L.-L. Du, W.-L. Chang, and X.-M. Tao, Thermoelectric properties of 2D semiconducting Pt_2CO_2, Phys. Scr. 97, (2022), 085706. https://doi.org/10.1088/1402-4896/ac7fc2